The origin of ferromagnetism in ^{57}Fe-doped NiO

2007 J. Phys.: Condens. Matter 19 436203

(http://iopscience.iop.org/0953-8984/19/43/436203)

IOP PUBLISHING JOURNAL OF PHYSICS: CONDENSED MATTER

J. Phys.: Condens. Matter **19** (2007) 436203 (25pp) doi:10.1088/0953-8984/19/43/436203

The origin of ferromagnetism in ^{57}Fe-doped NiO

A P Douvalis[1,2,3], L Jankovic[2] and T Bakas[2]

[1] Department of Materials Science and Engineering, University of Ioannina, PO Box 1186, 45110 Ioannina, Greece
[2] Physics Department, University of Ioannina, PO Box 1186, 45110 Ioannina, Greece

E-mail: adouval@cc.uoi.gr

Received 7 May 2007, in final form 31 July 2007
Published 26 September 2007
Online at stacks.iop.org/JPhysCM/19/436203

Abstract

The origin of ferromagnetism observed in 2 at.% ^{57}Fe-doped NiO samples is investigated. A precursor was produced from the co-precipitation of stoichiometric ^{57}Fe and Ni nitrate solutions, and the 2% ^{57}Fe-doped NiO samples were prepared by heating this precursor in air at temperatures between 673 and 873 K, for 1–25 h. X-ray diffraction, scanning electron microscopy, magnetization measurements and ^{57}Fe Mössbauer spectroscopy were used to study the properties of the prepared compounds. The samples are composed of crystalline nanoparticles with average sizes between 9 and 29 nm, depending on the heating conditions. Magnetization measurements show the appearance of room-temperature ferromagnetism for samples heated both at 673 and 873 K. The ^{57}Fe Mössbauer spectroscopy results indicate that this ferromagnetism is related to $Ni^{57}Fe_2O_4$ ferrimagnetic impurities for the samples heated at 873 K and to finite-size effects for the samples heated at 673 K. The $Ni^{57}Fe_2O_4$ impurities interact magnetically with the antiferromagnetic ^{57}Fe-doped NiO matrix and it is proposed that they result from a diffusion-type process of $^{57}Fe^{3+}$ ions during the heat treatment of the precursor.

1. Introduction

During the last few years there have been several theoretical and experimental reports on the appearance of ferromagnetism in technologically important semiconducting compounds when they are doped with small amounts of transition metal (TM) ions [1]. This new category of compounds form the so-called diluted magnetic semiconductor (DMS) family. The task of combining both ferromagnetic and semiconducting properties together with optical transparency in one (or several) compound(s) could lead to a new era for synthetic materials, which could be used as bases for a variety of magneto-electronic and opto-magneto-electronic device applications [2]. A number of these reports focus on binary oxide semiconductors like

[3] Author to whom any correspondence should be addressed.

TiO_2 [3], SnO_2 [4], ZnO [5], In_2O_3 [6], Cu_2O [7], CeO_2 [8] doped with small percentages of TM ions like Co, Fe, Mn, V, Cr, and Cu. The host materials in bulk form, prior to doping with the TM, show diamagnetic properties at room temperature (RT), while after doping the resulting compounds gain large values of magnetic moment per TM ion at RT, as well as Curie temperature (T_C) values of several degrees above RT.

There are recent reports on the appearance of RT ferromagnetism in a different system: NiO doped with 1–2 at.% Fe [9, 10]. Contrary to the above oxide systems, pure bulk NiO is an antiferromagnetic insulator at RT, with a band gap of ≈4.0 eV [11] and a Néel temperature (T_N) of 523 K [12]. The authors in these works [9, 10] report large average magnetic moments per Fe ion (around 0.38 μ_B/Fe ion) for their samples and ferromagnetic hysteresis loops from 78 K up to RT, which they claim that they could be extended at elevated temperatures, according to their magnetization versus temperature measurements. They justify their findings in the frame of non-impurity ferromagnetic clusters within the grains of the material, formed by regions of the NiO structure that are enriched in Fe^{3+} ions. They also propose that the electronic charge imbalance between Fe^{3+} and Ni^{2+} and the defects produced by the introduction of the Fe^{3+} ions in the NiO structure is thought to play a vital role on the appearance of ferromagnetism, based on the idea of carrier-mediated ferromagnetic interactions [1] between Fe^{3+} ions.

Taking into consideration that new reports on DMS systems are a very important issue on the way to establishing the origin of ferromagnetism in these compounds, we discuss in this paper our results on the structural and magnetic properties of 2 at.% ^{57}Fe-doped NiO samples, produced following the same chemical preparation route as in the above-mentioned works [9, 10]. We include the ^{57}Fe Mössbauer spectroscopy technique in our studies, which is one of the most specialized methods for giving important atomic-level information for the structural, electronic and magnetic properties of the iron ions present in the samples [13].

2. Experimental details

Samples of nominal $Ni_{0.98}{}^{57}Fe_{0.02}O$ compositions were prepared by the co-precipitation technique. In particular, stoichiometric quantities of high-purity metallic Fe (Chemgas 99.97%) 95.95% ^{57}Fe enriched and $Ni(NO_3)_2{\cdot}6H_2O$ (Aldrich 99.999%) were dissolved in pure HNO_3 and double-distilled water, respectively. The two solutions were mixed with addition of NH_4HCO_3 in order to keep the pH ≈8 at RT. The precipitated solid was washed several times with distilled water, centrifuged and dried in air at RT in order to produce the solid precursor. The resulting amorphous precursor was then heated at several temperatures from 673 to 873 K in air for various heating times from 1 to 25 h, in order to study the influence of the heating conditions (temperature and time) on the structural and magnetic properties of the prepared materials. To distinguish the samples according to their preparation conditions we refer to them by ascribing the heating temperature (in kelvin) and time (in hours) separated by a slash: for example, (673/1). To clarify our findings further (see the following) we prepared samples of pure NiO and $NiFe_2O_4$ phases following the same chemical preparation route as for the 2% ^{57}Fe-doped NiO samples, using stoichiometric quantities of high-purity $Ni(NO_3)_2{\cdot}6H_2O$ (Aldrich 99.999%) and $Fe(NO_3)_3{\cdot}9H_2O$ (Aldrich 99.99+%). The resulting NiO precursor was heated at 873 K for 4 h to produce pure NiO. The corresponding $NiFe_2O_4$ precursor was heated at 1173 K for 12 h and at 873 K for 1 and 4 h in order to produce $NiFe_2O_4$ samples with different particle sizes.

Powder x-ray diffraction (XRD) patterns of the precursors and the heated samples were collected on a Bruker D8-Advance diffractometer using Cu Kα radiation. All diffraction patterns were collected using a dwell time of 6 s per 2θ step with a step of 0.02°. Scanning electron microscopy (SEM) with energy dispersive x-ray (EDX) analysis measurements

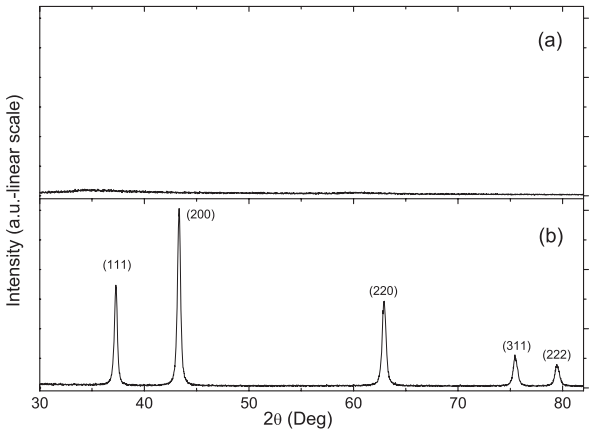

Figure 1. X-ray diffraction patterns of the 2% ^{57}Fe-doped NiO dried precursor (a) and sample (873/4) (b). The (*hkl*) indices of the diffraction planes of the FCC structure are also indicated in (b). The intensity axis is given in linear scale and both patterns are scaled at the same intensity limits.

(OXFORD, Link ISIS 300) were performed on selected 2% ^{57}Fe-doped NiO samples in a JEOL JSM-5600 microscope operated at 20 kV. Magnetization measurements of all samples were collected using a vibrating sample magnetometer (VSM) (LakeShore 7300), equipped with a low-temperature cryostat (Janis). ^{57}Fe Mössbauer spectra (MS) of all iron-containing samples were collected in transmission geometry at RT and 77 K, using a constant-acceleration Mössbauer spectrometer equipped with a ^{57}Co(Rh) source kept at RT, and a liquid N_2 bath Mössbauer cryostat (OXFORD). Velocity calibration of the spectrometer was carried out using metallic α-iron at RT and 77 K.

3. Experimental results and discussion

3.1. X-ray diffraction

Figure 1 shows the XRD patterns of the RT dried 2% ^{57}Fe-doped NiO precursor and the sample prepared by heating this precursor at 873 K for 4 h. The XRD pattern of the precursor is characteristic of an amorphous material, while the specific heat treatment gives a sample (873/4) which is a crystalline material with the characteristic NiO face-centered cubic (FCC) structure [14–18][4]. No impurity phase in the XRD pattern of the (873/4) sample is detectable with the intensity axis given in linear scale. However, since the segregation of secondary phases, that might give a contribution to ferromagnetic signals in DMSs, is a very important issue [19, 20], and in order to enhance the possible contribution of any minor impurity phase present in the samples, the intensity of which might have not been distinguished from the XRD background in a linear intensity scale due to the high intensity contribution of the dominant FCC phase, it is better to represent the XRD data with the intensity axis given in logarithmic scale.

Thus in figure 2 we present the XRD patterns of all the 2% ^{57}Fe-doped NiO prepared samples after the heat treatments of the precursor under the conditions indicated, with the

[4] It is known that NiO shows a symmetry lowering from the FCC structure (space group *Fm3m*) to the hexagonal structure (space group $R\bar{3}m$) below T_N (see [16–18]). However, the distortion of the FCC structure at RT is so small that for most of the studies of this material, including the present one, it is not detectable in the XRD patterns and can be neglected (see [14, 15]).

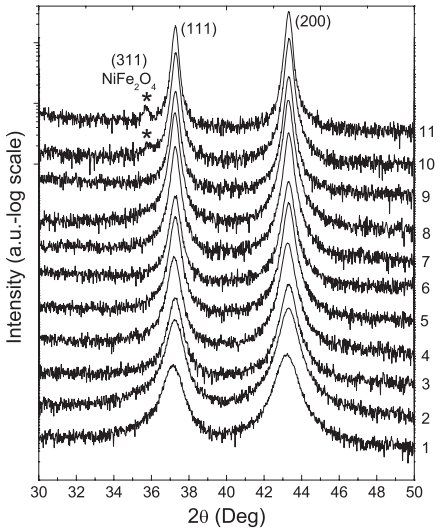

Figure 2. X-ray diffraction patterns of the 2% ^{57}Fe-doped NiO samples prepared by heating the corresponding precursor at different temperatures and for different times. Each number corresponds to a different sample indicated by its preparation conditions (see the text). 1: (673/1), 2: (673/5), 3: (673/25), 4: (773/1), 5: (793/2), 6: (823/1), 7: (823/4), 8: (873/1), 9: (873/4), 10: (873/12) and 11: (873/24). The intensity axis is given in logarithmic scale and each pattern is scaled at the same intensity limits. The (*hkl*) indices of the diffraction planes (111) and (200) of ^{57}Fe-doped NiO and (311) of $NiFe_2O_4$ (denoted by the *) are also indicated.

intensity axis given in logarithmic scale. The patterns show that all the prepared samples are crystalline materials and have a dominant contribution of the characteristic NiO FCC structure. From these patterns we can extract information on the morphology and average particle size, as well as on the presence of impurity phases in the samples.

3.1.1. Particle size and unit cell volume expansion. A broadening of the diffraction peaks for the low-temperature heated 2% ^{57}Fe-doped NiO samples is apparent, which indicates small particle size. In order to determine the average particle size t, we have taken into account the Scherrer formula [21],

$$t = \frac{0.9\lambda}{B\cos\theta_B},$$

applied on the (200) diffraction peak of the ^{57}Fe-doped NiO in the cubic $Fm3m$ space group. In this formula, $\lambda = 0.1542$ nm, the wavelength of the Cu Kα radiation, θ_B is the Bragg angle and B the peak's full width at half maximum (FWHM). The results are listed in table 1. It is evident that the particle size increases with increasing heating temperature or time. In particular, the samples heated at 673 K have average particle sizes below or just above 10 nm.

Another characteristic feature of the XRD patterns is a small shift in the position of the diffraction peaks towards lower 2θ values as the heating temperature or time decreases, which indicates a change in the FCC unit cell constant. This shift, according to the values of table 1, must be related to the average particle size. Indeed, figure 3 shows the dependence of the FCC ^{57}Fe-doped NiO unit cell volume and lattice constant, as resulting from the Rietveld refinements of the corresponding XRD patterns using the GSAS package [22], with respect to the average particle size. The cell volume is relatively constant for particles with average sizes from ≈30 to 20 nm, but increases abruptly for the smaller particles. This phenomenon is also observed in

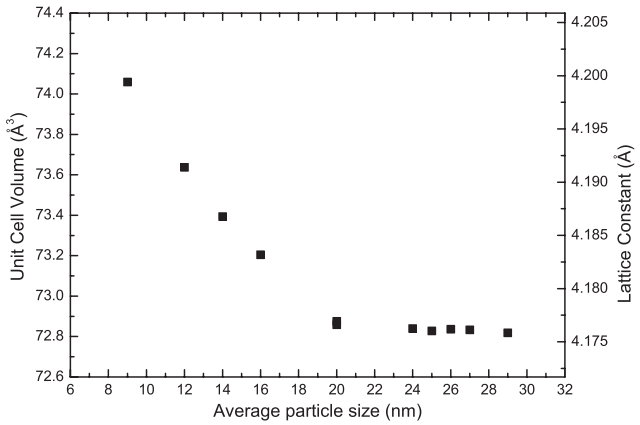

Figure 3. Variation of the volume and the lattice constant of the FCC unit cell of the 2% ^{57}Fe-doped NiO samples as resulting from Rietveld refinements of the corresponding XRD patterns, relative to their average particle size evaluated using the Scherrer formula.

Table 1. Average particle sizes of the 2% ^{57}Fe-doped NiO samples prepared at different heating temperatures and times, as resulting from the Scherrer formula. The number in parentheses is the standard deviation referred to the last digit for each value.

Temperature (K)	Time (h)	Average size t (nm)
673	1	9(1)
673	5	12(1)
673	25	14(1)
773	1	16(1)
793	2	20(2)
823	1	20(2)
823	4	24(2)
873	1	26(3)
873	4	25(3)
873	12	27(3)
873	24	29(4)

other pure NiO nanoparticle systems [20] and is suggested to influence the magnetic properties of the nanoparticles prepared in the present work (see the following discussion).

3.1.2. Impurity phases detected by XRD. It is evident from figure 2 that even after taking several hours of XRD scans of the samples heated from 673 to 823 K for all heating times and the samples heated at 873 K up to 4 h, there is no indication of appearance of any additional diffraction peak corresponding to a secondary impurity phase. However, it is important to notice that the detection limit of an individual crystalline phase in the samples with this technique is limited and relates to the specific resolution of the diffractometer, as well as to the quantity, quality of crystallization and particle size of the phase to be detected in the sample [23]. It is also important that the XRD patterns of the samples heated at 873 K for 12 and 24 h (873/12–24) indeed show the presence of an additional diffraction peak belonging to an impurity phase (marked by the star in figure 2), which is the (311) peak of the strong ferrimagnetic inverse spinel $NiFe_2O_4$, with T_C of 858 K [24].

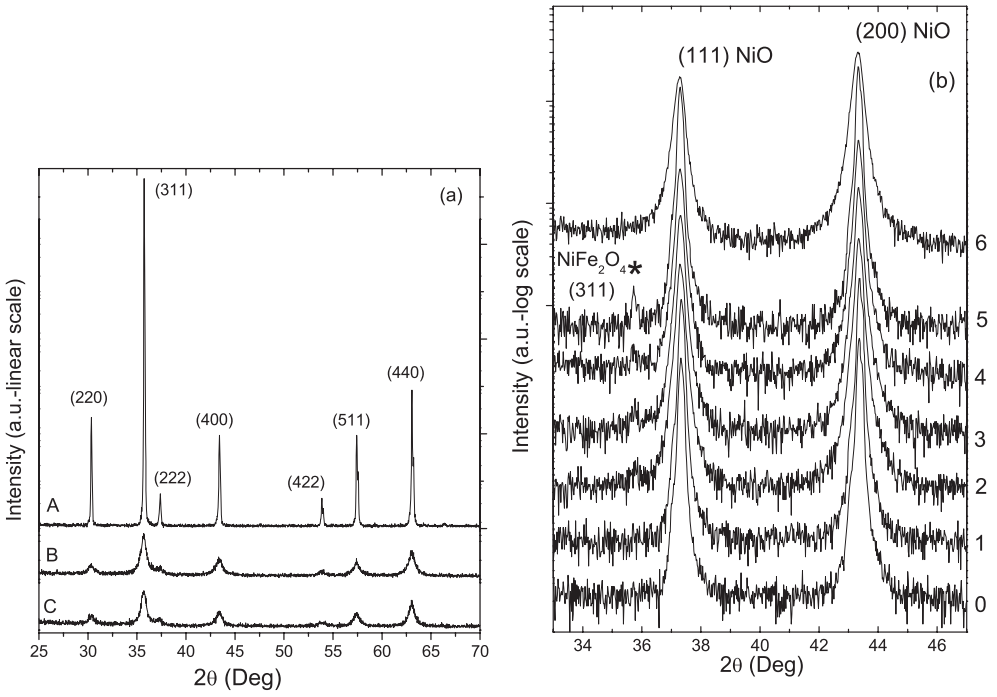

Figure 4. (a) X-ray diffraction patterns of the $NiFe_2O_4$ samples prepared using the same chemical route as for the ^{57}Fe-doped NiO samples. A, B and C denote the different $NiFe_2O_4$ samples (see the text). The intensity axis is given in linear scale and the (*hkl*) indices of the diffraction planes are also indicated. Each pattern is scaled at the same intensity limits. (b) X-ray diffraction patterns of the $NiFe_2O_4$/NiO mixture samples with different wt% of $NiFe_2O_4$ in NiO. 1: 0.1 wt%, 2: 0.2 wt%, 3: 0.3 wt%, 4: 0.4 wt%, 5: 0.5 wt%. For comparison the patterns of 0: pure NiO and 6: 2% ^{57}Fe-doped NiO sample (873/4) are also given. The intensity axis is given in logarithmic scale and each pattern is scaled at the same intensity limits. The (*hkl*) indices of the diffraction planes (111) and (200) of NiO and (311) of $NiFe_2O_4$ (denoted by *) are also indicated.

In order to have an estimate of the wt% detection limit of this impurity phase in our samples using the x-ray diffraction technique, we prepared pure NiO and $NiFe_2O_4$ phases using the same preparation route as for the 2% ^{57}Fe-doped NiO samples. For the NiO preparation we used the same heating temperature and time conditions to treat the NiO precursor as we did for the (873/4) sample, while three samples of the $NiFe_2O_4$ phase resulted from heating the corresponding precursor at 1173 for 12 h ($NiFe_2O_4$-A) and at 873 K for 1 h ($NiFe_2O_4$-B) and 4 h ($NiFe_2O_4$-C). From these samples we prepared mechanical mixtures in an agate mortar, with several wt% of $NiFe_2O_4$-A in NiO, and collected their x-ray diffractograms using the same experimental scan conditions as for the 2% ^{57}Fe-doped NiO samples, in an effort to simulate the coexistence of the $NiFe_2O_4$ and NiO phases in them. The x-ray diffractograms of the separate phases and mixtures are shown in figure 4.

It is apparent that the NiO phase has the same characteristics as the (873/4) sample and that the different $NiFe_2O_4$ samples have different widths in their diffraction peaks, indicating different particle sizes according to their preparation conditions. From the Scherrer formula [21], we estimated the average particle size of the pure NiO sample to be 45 nm, and 51 nm, 11 nm, and 12 nm for the $NiFe_2O_4$-A, $NiFe_2O_4$-B, and $NiFe_2O_4$-C samples, respectively. We used the $NiFe_2O_4$-A sample to prepare the $NiFe_2O_4$/NiO mixtures, as this

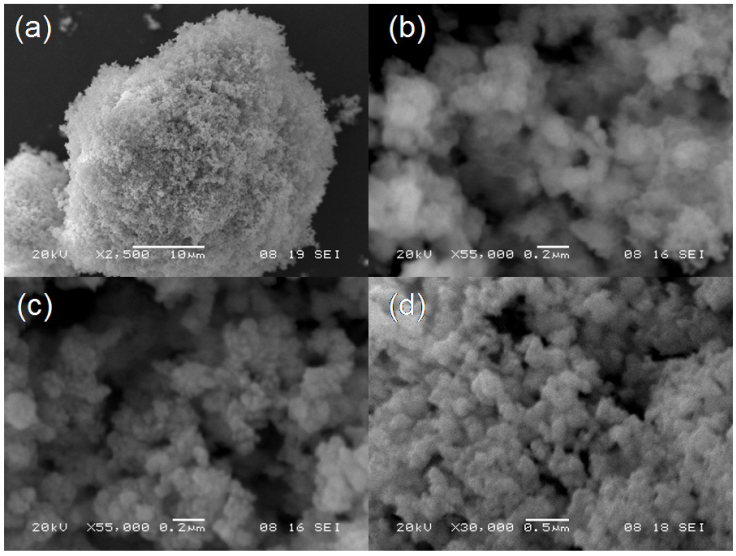

Figure 5. Scanning electron microscopy images of selected 2% ^{57}Fe-doped NiO samples. The length scale is given in each picture. (a) Sample (793/2), (b) sample (673/1), (c) sample (793/2), (d) sample (873/1).

sample has the larger average particle size (sharpest diffraction peaks), and therefore the best crystallization, in order to estimate the lower wt% detection limit of this phase in the mixtures. It follows that for even more nanostructured and less well-crystallized $NiFe_2O_4$ phases, like the other two $NiFe_2O_4$-B and $NiFe_2O_4$-C samples which have broader and less intense diffraction peaks, this limit would be even higher. As shown in figure 4, the estimated wt% detection limit of the 'bulk-like' $NiFe_2O_4$ phase in NiO in these mixtures using the XRD technique with the above measurement conditions is between 0.1 and 0.2 wt%. Thus it is evident that the presence or not of any secondary impurity phase like $NiFe_2O_4$ below the 0.2 wt% limit in our samples cannot solely rest on the XRD results.

3.2. SEM and EDX analyses

We performed SEM analyses of selected samples (673/1), (793/2) and (873/1). The results are shown in figure 5. As can be seen, all samples are composed of assemblies of very small round-shaped particles. A distribution of particle sizes is observed and it seems to be broader for the (793/2) sample. The average particle size of the low-temperature heated (673/1) sample is below 20 nm, and as the temperature increases the average particle diameter increases, in good agreement with the results deduced from the XRD patterns. In the EDX analyses we found no region in any of these samples with a $\frac{\text{Fe}}{\text{Ni}}$ ratio different form an average of $\frac{2.4(\pm 0.1)}{97.6(\pm 0.1)}$. Thus it is very difficult to distinguish the presence of any impurity phase, like $NiFe_2O_4$, in our samples using SEM and EDX analysis at this magnification.

3.3. Magnetization measurements

Figures 6–8 show the specific magnetization versus applied magnetic field (σ versus H) measurements of the 2% ^{57}Fe-doped NiO samples recorded at RT, after subtracting the diamagnetic contribution of the sample holder.

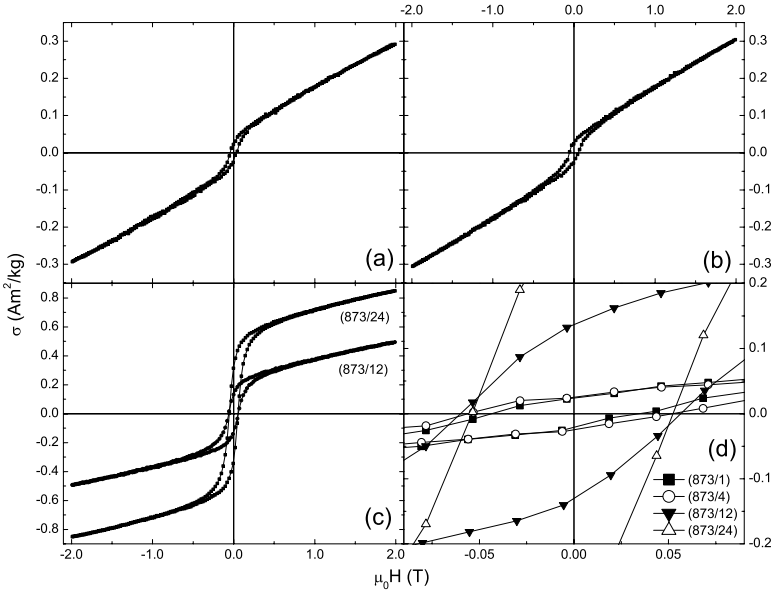

Figure 6. Room-temperature magnetization loops of the 2% ^{57}Fe-doped NiO samples: (a) (873/1), (b) (873/4), (c) (873/12) and (873/24), (d) magnification of the −0.10 to +0.10 T applied field area.

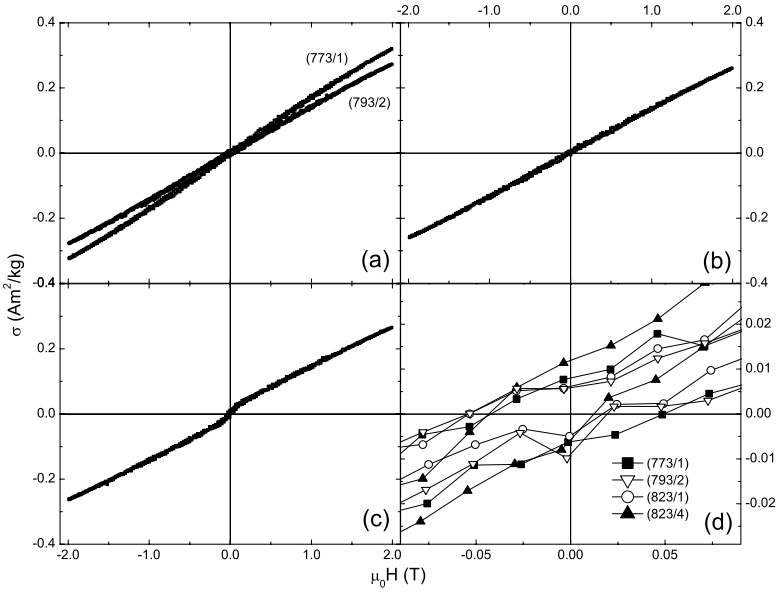

Figure 7. Room-temperature magnetization loops of the 2% ^{57}Fe-doped NiO samples: (a) (773/1) and (793/2), (b) (823/1), (c) (823/4), (d) magnification of the −0.10 to +0.10 T applied field area.

It is evident from figure 6 that all the (873/1–24) samples show ferromagnetic signals with clear hysteresis. The shape of the loops is characteristic of a combination of two parts, one of a minority strong ferromagnetic or ferrimagnetic phase and the other of a dominant

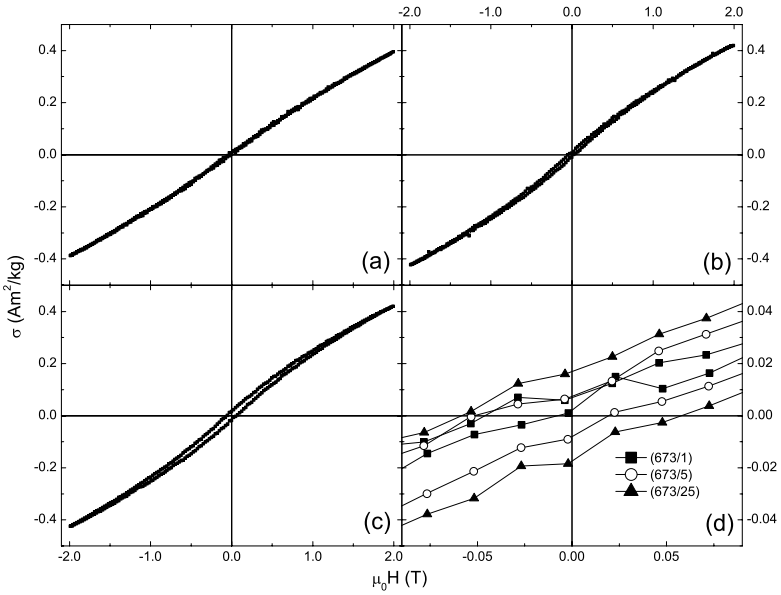

Figure 8. Room-temperature magnetization loops of the 2% ^{57}Fe-doped NiO samples: (a) (673/1), (b) (673/5), (c) (673/25), (d) magnification of the −0.10 to +0.10 T applied field area.

antiferromagnetic phase. The contribution of the strong ferromagnetic part decreases when the heating time at 873 K decreases. The remanence (σ_R) and maximum magnetization at $\mu_0 H = 2$ T (σ_{2T}) from 0.320 A m^2 kg^{-1} and 0.849 A m^2 kg^{-1} for the (873/24) sample reduce to 0.024 A m^2 kg^{-1} and 0.291 A m^2 kg^{-1}, respectively, for the (873/1) sample. The coercivities for all samples prepared at 873 K are about 40–60 mT. In figure 7(c) the magnetization loop for the (823/4) sample looks similar to that of the (873/1) sample of figure 6(a), but the contribution of the strong ferromagnetic phase is considerably reduced, as the σ_R of the former (≈0.009 A m^2 kg^{-1}) is decreased to less than one half of the latter. However, the σ_{2T} value of the (823/4) sample shows a more restrained decrease to ≈0.265 A m^2 kg^{-1}. In figures 7(a) and (b) the variation of magnetization for the (773/1), (793/2) and (823/1) samples is linear, showing only the characteristic antiferromagnetic behavior, indicating the absence of any strong ferromagnetic phase contribution. σ_{2T} has its minimum for the (823/1) sample (≈0.260 A m^2 kg^{-1}), but increases again slightly and gradually as the heating temperature decreases, to $\sigma_{2T} \approx 0.273$ A m^2 kg^{-1} for the (793/2) and $\sigma_{2T} \approx 0.320$ A m^2 kg^{-1} for the (773/1) samples.

In figure 8 a new shape of a weak ferromagnetic signal appears for the (673/1–25) samples, in combination with the dominant antiferromagnetic contribution which is still present. This new ferromagnetic contribution is quite different from the strong ferromagnetic contribution of the high-temperature heated samples of figure 6. The new characteristic is the high irreversibility of the magnetization loop which is more apparent in the (673/25) sample, where the ascending and descending applied field curves are joined at ≈±1.4 T. This irreversibility is considerably reduced as the heating time shortens at this heating temperature to ≈±0.8 T for the (673/5) sample and vanishes almost completely for the (673/1) sample. On the other hand, as the heating time increases, the linear antiferromagnetic contribution decreases and a tendency towards a saturation-type behavior appears. It is characteristic that samples (673/5) and (673/25) have the same σ_{2T} values ≈0.420 A m^2 kg^{-1}, and for sample (673/1) σ_{2T} drops just to ≈0.394 A m^2 kg^{-1}. A decrease in the coercive field of the samples is observed as the

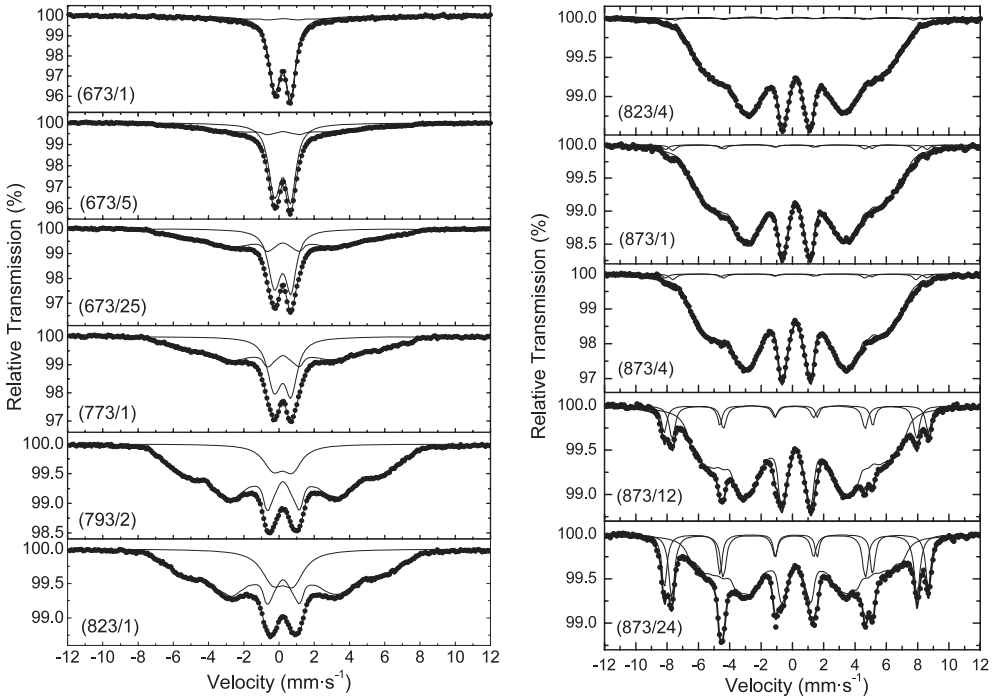

Figure 9. Room-temperature ^{57}Fe Mössbauer spectra of the 2% ^{57}Fe-doped NiO samples. Each spectrum is identified by the sample's name. The dots correspond to experimental points and the continuous lines to the different contributions used to fit the spectra.

heating time at 673 K decreases, from 60 mT for (673/25) to 23 mT for (673/1), while a shift of the loops towards the negative applied field values is detected, especially for the (673/1) sample, which is however reduced as the heating time increases at this temperature. The values of σ_R for the samples heated at 673 K lie in the range of the σ_R values of the 773–793 K heated samples ($\approx$0.007 A m^2 kg^{-1}), except for the (673/25) sample, the value of which reaches $\approx$0.017 A m^2 kg^{-1}.

3.4. ^{57}Fe Mössbauer spectroscopy

The results of the magnetization measurements suggest the presence of a strong ferromagnetic component for the highest-temperature and a weaker one for the lowest-temperature heated samples, respectively, while intermediate heating temperatures produce samples with characteristic antiferromagnetic behavior, relieved from any ferromagnetic contribution. One could attribute the ferromagnetism found for the highest-temperature heated samples to an intrinsic property of the iron-doped NiO phase, as already reported by Wang *et al* [9] and Lin *et al* [10]. The definite presence of the $NiFe_2O_4$ ferrimagnetic phase in the XRD patterns of the (873/12–24) samples makes this argument quite uncertain, if not feeble. However, for the shorter heating time samples at this temperature (873/1–4) or at 823 K (823/4), there is no clear evidence for the presence of this ferrimagnetic phase in the XRD patterns. To clarify this completely, another experimental method must be used to determine the origin of ferromagnetism in these samples. This is the reason that the most important result of this study comes from the ^{57}Fe Mössbauer spectroscopy measurements. MS of all 2% ^{57}Fe-doped NiO samples recorded at RT and 77 K are shown in figures 9 and 10, respectively, and the

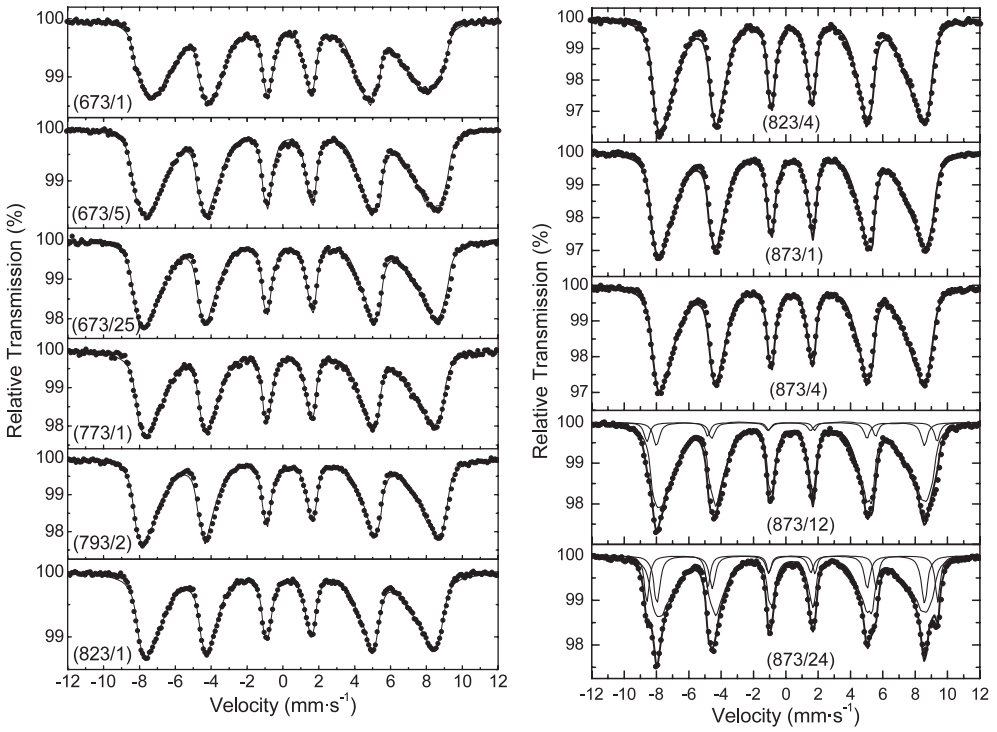

Figure 10. 77 K ^{57}Fe Mössbauer spectra of the 2% ^{57}Fe-doped NiO samples. Each spectrum is identified by the sample's name. The dots correspond to experimental points and the continuous lines to the different contributions used to fit the spectra.

Mössbauer parameters (MPs) of the components used to fit these experimental data appear in tables 2 and 3.

In the RT spectra of the lower-temperature heated samples (673/1–25), a paramagnetic quadrupole doublet dominates, combined with a broad—but minor in absorption area—magnetically split part. The broad magnetic part gradually increases and becomes the majority of the absorption area of the spectrum as the sample's heating time and/or temperature increases. An asymmetry in the absorption lines of the quadrupole doublet is observed, as the positive velocity line is more intense and sharper than the negative velocity one. However, this asymmetry seems to be reduced for the doublets appearing in the RT MS of the (793/2) and (823/1) samples. Thus to reproduce the experimental data adequately we used a quadrupole split component with asymmetric absorption lines in order to simulate the intensity asymmetry of the paramagnetic contribution and a combination of magnetically split components to describe the broad magnetic part in each spectrum.

For the set of magnetic components reproducing the broad magnetic part of each spectrum, a Lorentzian-type distribution of hyperfine magnetic field (B_{hf}) values with a width of ΔB_{hf} was allowed for each component, in order to better describe the line broadening. The isomer shift (IS) values of all components (given relative to α-Fe at RT) indicate that all iron ions corresponding to these contributions (both paramagnetic and magnetic) are in the Fe^{3+} high-spin ($S = 5/2$) state. It is evident from the IS values listed in tables 2 and 3 that the Fe^{3+} character of these contributions to the MS is valid for all ^{57}Fe-doped NiO samples prepared in this work.

Table 2. Mössbauer parameters as resulting from the best fits of the room-temperature spectra of the 2% ^{57}Fe-doped NiO samples. $\Gamma/2$, IS, Δ, 2ε, B_{hf}, ΔB_{hf} and A correspond to the half line-width, isomer shift, quadrupole splitting, quadrupole shift, hyperfine magnetic field, width of the distribution of B_{hf} and relative absorption area, respectively, of the components used to fit the spectra. (M), (SPM), (A) and (B) denote magnetic, superparamagnetic, A site and B site, respectively. The values of Fe^{3+} in NiO (M) contributions are weighted averages (with respect to their absorption areas) of the assembly of components used to fit this part of the spectrum (see the text). The $\Gamma/2$ values of the SPM components are also weighted averages. Typical errors are ± 0.02 mm s^{-1} for $\Gamma/2$, IS, Δ and 2ε, ± 0.5 T for B_{hf} and ΔB_{hf}. The numbers in parentheses for A are standard deviations corresponding to the last digit for each value.

Sample	Component	$\Gamma/2$ (mm s^{-1})	IS (mm s^{-1})	2ε or Δ (mm s^{-1})	B_{hf} (T)	ΔB_{hf} (T)	A (%)
(673/1)	Fe^{3+} in NiO (M)	0.25	0.33	0.00	23.8	2.6	19.4(2)
	Fe^{3+} in NiO (SPM)	0.32	0.31	0.90	—	—	80.6(6)
(673/5)	Fe^{3+} in NiO (M)	0.25	0.33	0.00	23.1	2.7	38(2)
	Fe^{3+} in NiO (SPM)	0.34	0.31	0.92	—	—	61(2)
(673/25)	Fe^{3+} in NiO (M)	0.24	0.33	0.00	25.5	2.5	61.0(9)
	Fe^{3+} in NiO (SPM)	0.35	0.31	0.94	—	—	39(1)
(773/1)	Fe^{3+} in NiO (M)	0.24	0.33	0.00	25.3	2.6	66(2)
	Fe^{3+} in NiO (SPM)	0.40	0.31	0.95	—	—	33(2)
(793/2)	Fe^{3+} in NiO (M)	0.23	0.34	0.01	26.7	2.5	87.0(9)
	Fe^{3+} in NiO (SPM)	0.63	0.31	1.09	—	—	13.0(7)
(823/1)	Fe^{3+} in NiO (M)	0.23	0.34	0.01	27.1	2.5	79.6(7)
	Fe^{3+} in NiO (SPM)	0.72	0.33	1.16	—	—	20(1)
(823/4)	Fe^{3+} in NiO (M)	0.23	0.34	0.01	27.4	2.4	99.0(4)
	$NiFe_2O_4$ (A)	0.21	0.23	0.01	47.4	0.1	0.56(1)
	$NiFe_2O_4$ (B)	0.15	0.36	0.00	51.1	0.3	0.36(1)
(873/1)	Fe^{3+} in NiO (M)	0.23	0.34	0.01	28.1	2.4	97.6(7)
	$NiFe_2O_4$ (A)	0.21	0.23	0.01	48.4	0.1	1.4(4)
	$NiFe_2O_4$ (B)	0.15	0.36	0.00	52.1	0.3	1.0(3)
(873/4)	Fe^{3+} in NiO (M)	0.22	0.34	0.01	29.2	2.2	97.6(3)
	$NiFe_2O_4$ (A)	0.21	0.23	0.01	48.4	0.1	1.5(1)
	$NiFe_2O_4$ (B)	0.15	0.36	0.00	52.1	0.3	0.9(1)
(873/12)	Fe^{3+} in NiO (M)	0.22	0.34	0.01	29.7	2.2	85.8(5)
	$NiFe_2O_4$ (A)	0.21	0.23	0.01	48.7	0.1	8.2(2)
	$NiFe_2O_4$ (B)	0.15	0.36	0.00	52.6	0.3	6.0(2)
(873/24)	Fe^{3+} in NiO (M)	0.22	0.34	0.01	29.6	2.2	68.0(7)
	$NiFe_2O_4$ (A)	0.21	0.23	0.01	48.9	0.1	18.0(6)
	$NiFe_2O_4$ (B)	0.15	0.36	0.00	52.6	0.3	14.0(5)

No contribution from any other different component to the RT MS of the samples heated at temperatures up to 823 K and for up to 1 h is observed. For all samples that exceeded these heating conditions, a new additional magnetic contribution appears in the MS, which gradually

Table 3. Mössbauer parameters as resulting from the best fits of the 77 K spectra of the 2% ^{57}Fe-doped NiO samples. The values of Fe^{3+} in NiO and Fe^{3+} in NiO and $NiFe_2O_4$ contributions are weighted averages (with respect to their absorption areas) of the assembly of components used to fit this part of the spectrum (see the text). (A) and (B) denote A site and B site, respectively. Typical errors are ± 0.02 mm s^{-1} for $\Gamma/2$, IS and 2ε, ± 0.5 T for B_{hf} and ΔB_{hf}. The numbers in parentheses for A are standard deviations corresponding to the last digit for each value.

Sample	Component	$\Gamma/2$ (mm s^{-1})	IS (mm s^{-1})	2ε (mm s^{-1})	B_{hf} (T)	ΔB_{hf} (T)	A (%)
(673/1)	Fe^{3+} in NiO	0.23	0.45	0.00	44.5	1.4	100(1)
(673/5)	Fe^{3+} in NiO	0.23	0.45	−0.01	47.7	1.4	100(2)
(673/25)	Fe^{3+} in NiO	0.22	0.45	−0.02	48.0	1.2	100(2)
(773/1)	Fe^{3+} in NiO	0.22	0.43	−0.02	47.2	1.7	100(2)
(793/2)	Fe^{3+} in NiO	0.23	0.45	0.01	48.4	1.1	100(2)
(823/1)	Fe^{3+} in NiO	0.22	0.43	0.00	47.2	1.7	100(1)
(823/4)	Fe^{3+} in NiO and $NiFe_2O_4$	0.22	0.45	−0.01	48.1	1.3	100(2)
(873/1)	Fe^{3+} in NiO and $NiFe_2O_4$	0.21	0.46	−0.01	48.7	1.2	100(2)
(873/4)	Fe^{3+} in NiO and $NiFe_2O_4$	0.22	0.45	0.01	48.4	1.2	100(2)
(873/12)	Fe^{3+} in NiO	0.21	0.46	−0.01	48.7	1.2	86(2)
	$NiFe_2O_4$ (A)	0.22	0.36	0.06	51.7	0.1	8(1)
	$NiFe_2O_4$ (B)	0.16	0.48	0.02	55.9	0.3	6(1)
(873/24)	Fe^{3+} in NiO	0.21	0.46	−0.01	48.7	1.2	68(2)
	$NiFe_2O_4$ (A)	0.21	0.38	0.06	51.6	0.1	18(1)
	$NiFe_2O_4$ (B)	0.15	0.50	0.02	56.1	0.2	14(1)

increases its absorption area as the heating temperature and time increase. It is clear that this contribution corresponds to Fe ions with completely different characteristics compared to the characteristics of the iron ions in the broad paramagnetic/magnetic contributions. This new contribution appears at around the same velocity positions, but with quite increased intensity, in the MS of the highest-temperature and longer-time heated samples (873/12–24), where it can be clearly seen that it is actually composed of two components. The best fits of this high hyperfine magnetic field components for these two samples gives MPs which correspond to the Fe^{3+} tetrahedral (A) and octahedral (B) oxygen coordinated sites, respectively, of the inverse spinel $NiFe_2O_4$ phase [25–27]. This confirms the XRD data of the (873/12–24) samples, where we have indeed found the presence of this phase as an impurity. In the RT MS of the samples with shorter heating time at 873 K, where there is no indication of the nickel ferrite in the XRD patterns, the contribution from this phase indeed appears, but with decreased intensity and absorption area. So, the above results indicate that the concentration of the strong ferrimagnetic nickel ferrite impurity phase in the samples is decreased as the heating time at

873 K decreases, is further reduced for the (823/4) sample and has completely disappeared for the (823/1) sample, in agreement with the results of their magnetization measurements.

At 77 K the MS show only magnetically split contributions with complete absence of any paramagnetic part for all samples. A combination of magnetic components was used to fit these spectra and the resulting MPs confirm the presence of only Fe^{3+} ions in all samples (see table 3). The resonant lines for all spectra at 77 K remain relatively broad; however, the broadening is decreased, compared with that of the magnetic components at RT. The Mössbauer components corresponding to the A and B sites of the $NiFe_2O_4$ phase can be undoubtedly detected at this temperature only in the MS of the (873/12–24) samples, where their contribution is quite significant. For the rest of the samples where this phase has been detected in the RT MS, the $NiFe_2O_4$ components coincide with the Mössbauer resonant lines of the broad magnetic components which posses the majority of the absorption area, due to the small absorption area of the former and to the increase in the B_{hf} values of the latter as a result of the decrease in measuring temperature.

4. Discussion

4.1. Samples with no $NiFe_2O_4$ impurities

The variation of the magnetization of the (673/1–25) samples with the applied field is characteristic of the weak ferromagnetism appearing in antiferromagnetic nanoparticle systems, a striking example of which is NiO nanoparticles [14, 20, 28–34]. The paramagnetic contributions appearing in the RT MS of the (673/1–25), (773/1), (793/2) and (823/1) samples are attributed to iron ions embedded in stoichiometric $Ni_{0.98}{}^{57}Fe_{0.02}O$ nanoparticles, which show superparamagnetic properties at RT [14]. The superparamagnetic nature of these nanoparticles is deduced by the absence of any paramagnetic contribution in the corresponding 77 K spectra. This absence is caused by the cessation of the fast thermal agitation of the sublattice magnetization (superparamagnetic relaxation) when the sample temperature drops below the blocking temperature (T_B) [35, 36]. It is known that this agitation causes the appearance of the superparamagnetic contribution in the MS, when the characteristic relaxation time τ for this procedure is significantly smaller than the characteristic Larmor precession time τ_L. In order to detect a B_{hf} of the order of 20.0–40.0 T, which is in the range of the B_{hf} values we find for the magnetic split components at RT, τ_L should be $\approx 10^{-8}$ s [37, 38]. On the other hand, the Mössbauer measuring time-window is $\tau_N \approx 1.4 \times 10^{-7}$ s [38]. Thus for the superparamagnetic particles both τ and τ_L are smaller than τ_N, and τ is also significantly smaller than τ_L. As τ is temperature dependent [35–39], when the temperature drops below T_B the value of τ for the particles that showed superparamagnetic properties at RT is increased and moves to values comparable or even higher than τ_L and τ_N. As a result, magnetic splitting also appears for these particles in the 77 K MS. However, when τ and τ_L are comparable, the shape of the absorption lines of the spectra is broad and more complex than in the slow relaxation limit, where $\tau \gg \tau_L, \tau_N$ [38].

If T_B is defined as the temperature at which the superparamagnetic and the magnetically split part of the MS have equal absorption areas [14], then T_B has a value between 77 K and RT for (673/1) and (673/5) samples, but higher than RT for (673/25), (773/1), (793/2), and (823/1) samples. The increase in the magnetic part at the expense of the superparamagnetic part for the RT MS of all samples as the heating time or temperature increases reflects the corresponding increase in T_B and is related to the particle size growth. In particular the superparamagnetic relaxation time τ depends on the temperature (as discussed above), as also on the magnetic anisotropy constant K and the volume of the particle V which is involved in

this procedure [35–39]. If we assume that K is more or less constant within a certain range of particle volumes, τ increases as V increases and becomes comparable to or larger than τ_L above a certain size limit. The particles with sizes above this limit contribute to the magnetic split part of the RT MS. So the increase in the absorption area of the magnetic components of the RT MS, with increasing heating time or temperature, indicates an increase of the part of the 2% ^{57}Fe-doped NiO samples that includes particles with sizes which overcome the superparamagnetic size limit at RT. Thus the average particle size increases, which is in agreement with the results deduced from the XRD and SEM analyses.

An estimation of the magnitude of τ can be made from the shape of the lines of the superparamagnetic component. As discussed section 3.4, a shape asymmetry is observed in the resonant lines of this doublet, especially for the low-temperature heated samples. This asymmetry is also observed in other antiferromagnetic nanoparticle systems at elevated temperatures [40] and is attributed to the fast superparamagnetic relaxation effect when the magnitude of τ is of the order of 10^{-10} s [41, 42]. The decrease of this asymmetry, as well as the increase in the line-width of this superparamagnetic doublet as the heating temperature or time increases (see table 2), indicates an increase in the magnitude of τ, relative to the 10^{-10} s value. This increase in τ is caused by the increase in the average particle size for this part of the sample (superparamagnetic particles) as a result of increasing heating temperature and time.

The presence of nanoparticles with sizes ≈10 nm for the (673/1–25) samples, confirmed from XRD, SEM and Mössbauer spectroscopy measurements, leads us to ascribe the weak ferromagnetism found in their magnetization behavior to finite-size effects, which include the following. (a) The uncompensated (Fe^{3+} or Ni^{2+}) spin moments appearing mainly on the surface of these $Ni_{0.98}Fe_{0.02}O$ nanoparticles [14, 31, 32]. (b) The multi-sublattice structure [30–32]. (c) The introduction of surface magnetic anisotropy related to the lower oxygen coordination number of surface Ni^{2+} or Fe^{3+} ions due to broken bond formation [43], as in the case of the corresponding pure NiO or $Ni_{0.995}{}^{57}Fe_{0.005}O$ nanoparticles. From the above results we come to the conclusion that for the (673/1–25), (773/1), (793/2) and (823/1) samples both paramagnetic and magnetic contributions to the RT MS can be attributed only to Fe^{3+} ions embedded in the NiO structure, substituting the Ni^{2+} ions and adapting the magnetic ordering of the Ni^{2+} sublattices, as in the case of 0.5% ^{57}Fe-doped NiO samples [14].

The relative decrease in coercivity as the heating time decreases for the samples heated at 673 K is related to the lattice expansion observed, as their corresponding average particle size decreases. This is also a characteristic of the weak ferromagnetism appearing in NiO nanoparticles, which shows a magnetic crossover effect with a peak in coercivity related to particle size [20, 30]. Also, the negative shift found in the magnetization loops of these samples is consistent with an analogous shift observed in NiO nanoparticles and is also attributed to finite-size effects [30]. The decrease of this shift with increasing heating time is related to the increase in particle size of the longer-heated samples at 673 K, which produces a lower surface to volume ratio, and thus reduces the contribution from these effects to the magnetization loop.

As the heating temperature of the samples increases above 673 K, the average particle size is further increased and the contribution of the weak ferromagnetic features—appearing mainly in the samples heated at 673 K—is decreased considerably for the (773/1), (793/2) and (823/1) samples. For these samples, as indicated by the analysis of their MS, only a minority part in each one shows superparamagnetic phenomena due to their small particle size at RT, while the other part containing the larger particles starts to have a ‘bulk-like’ behavior. These results are in agreement with the relative decrease in coercivity detected for NiO nanoparticles with increased sizes [20, 30], and indicate that the (673/25) sample should have a coercivity closer to the maximum value expected for these kinds of particles which can follow a magnetic crossover effect [20].

Another issue which demands further explanation is the broadening of the resonant lines of the MS, specially if one compares our MS with the corresponding MS of 0.5% ^{57}Fe-doped NiO nanoparticles [14]. This is related to several reasons. First, the substitution of Fe^{3+} for Ni^{2+} in the NiO structure affects the local ionic environment, because it requires the formation of one Ni^{2+} ion vacancy for every two Ni^{2+} ions substituted by Fe^{3+} ions in order to preserve the charge neutrality. This causes distortions on the first O^{2-} anion neighbor environment of the Fe^{3+} and Ni^{2+} octahedra, and also causes a variety of first and second cation neighbor environments for the inserted Fe^{3+} ions, introducing disorder in the NiO structure. Second, the distribution of particle sizes induces a distribution in T_B and τ values. Third, the decrease and distribution of the oxygen coordination number for the surface Fe^{3+} ions, due to broken bond formations, produces consequent differences in their magnetic interactions relative to the corresponding Fe^{3+} ions substituting core Ni^{2+} ions. Fourth, the most probable presence of a multi-sublattice, instead of the classic antiferromagnetic two-sublattice magnetic structure in the smaller nanoparticles, causes the appearance of a variety of magnetic interactions. Fifth, there is the presence of some interparticle magnetic interactions [44], as all our measurements were done in the as-prepared samples without grinding them; it is known that grinding could partially reduce magnetic coupling between particles [14]. Sixth, there is a possible presence of some degree of structural disorder of the ^{57}Fe-doped NiO nanoparticles, which reduces as the heating temperature or time increases. All the above reasons give rise to a distribution of MP values (mainly in B_{hf}, 2ε, and Δ) which influence the shape of the MS (both magnetic and paramagnetic components). It is also quite important to mention here that the shape of the broad magnetically split part of the Mössbauer spectrum recorded at RT is quite stable for each sample. However, a slight increase in the average B_{hf} values is observed as the heating temperature or time increases, which indicates an increase in the degree of crystallization and in the T_B of the system, as already mentioned. We can thus conclude that this part of the spectrum is relatively independent of both heating temperature and time, and only its proportion changes through the variation of the preparation conditions. Lowering the temperature from RT to 77 K will have a major influence only in the τ values; however, all other reasons describing the broadening of the Mössbauer resonant lines still remain active. Thus the spectra retain a line-broadening at 77 K, which is higher compared with the corresponding spectra of Bahl *et al* [14], due to the increased level of doping (four times higher) of Fe ions in our samples.

It is also worth noting here that we observe a quadrupole split component for the smallest in size 2% ^{57}Fe-doped NiO superparamagnetic nanoparticles instead of a singlet observed for the corresponding 0.5% ^{57}Fe-doped NiO nanoparticles by Bahl *et al* [14]. This indicates that the distortions of the FeO_6 octahedra in our 2% ^{57}Fe-doped NiO samples caused by the O^{2-} displacements are rather large, compared to the cubic symmetry observed for the corresponding FeO_6 octahedra of the samples of Bahl *et al*. The higher number of iron ions embedded in the NiO structure for the case of our samples, which produces a higher number of Ni^{2+} vacancies and thus larger displacements for the O^{2-} ions, is again responsible for these distortions. These displacements contribute to the breakdown of the local cubic symmetry of the FeO_6 octahedra, which in turn produces a non-zero quadrupole spitting for the superparamagnetic components in the MS.

4.2. Samples with detected $NiFe_2O_4$ impurities

Increasing the heating temperature from 823 to 873 K causes a further increase in particle size. So the 'bulk-like' antiferromagnetic shape of the magnetization loop of the $Ni_{0.98}{}^{57}Fe_{0.02}O$ phase, as shown for the (823/1) sample, is also expected to contribute to the corresponding loops of the (823/4) and (873/1–24) samples. However, for the latter samples the appearance

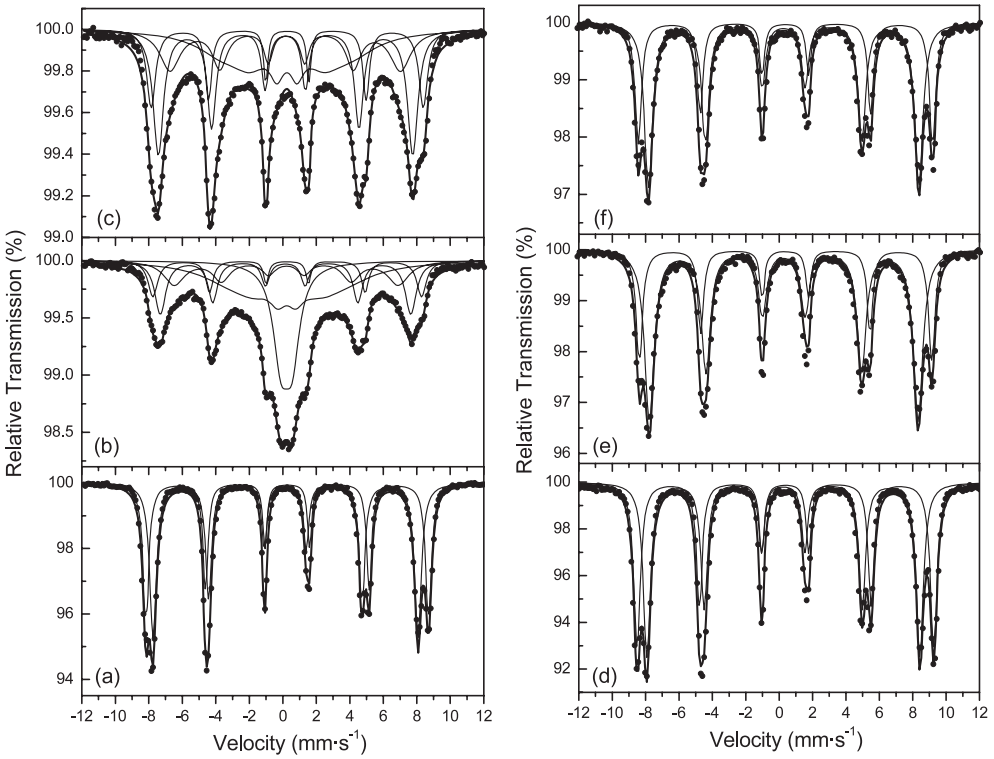

Figure 11. Room-temperature (left) and 77 K (right) ^{57}Fe Mössbauer spectra of the prepared $NiFe_2O_4$ samples (see the text): (a) and (d) $NiFe_2O_4$-A, (b) and (e) $NiFe_2O_4$-B, (c) and (f) $NiFe_2O_4$-C.

of the $NiFe_2O_4$ phase in their MS or/and the XRD patterns introduces the solid consideration of attributing the additional strong ferromagnetic signal detected in all magnetization loops to the presence of this ferrimagnetic impurity. For these samples it is characteristic that no line broadening for the two $NiFe_2O_4$ Mössbauer components is observed in their RT MS. Yet there is a small decrease in the B_{hf} values of these components as the heating time decreases from 24 to 1 h for the samples heated at 873 K, and the same is observed for the (823/4) sample. This small decrease in the B_{hf} values, compared to the expected 'bulk' values for $NiFe_2O_4$ [26], indicates the presence of very small particles of this impurity phase in the samples, as this phenomenon is a characteristic particle size effect in magnetic nanoparticles [35, 45].

It follows that the presence of even smaller in size superparamagnetic impurity $NiFe_2O_4$ nanoparticles in our 2% ^{57}Fe-doped NiO samples, heated in conditions higher then those of the (823/1) sample, cannot be undoubtedly excluded. This is because their contributions to the RT MS appear either as a broad superparamagnetic component positioned around the center of each spectrum or as a magnetic component with collapsing B_{fh}, and cannot be directly distinguished from all the other ^{57}Fe-doped NiO main-phase contributions. The shape and nature of these impurity contributions can be revealed by analyzing the MS recorded at RT and 77 K of the pure $NiFe_2O_4$-A, -B and -C samples prepared following the same chemical route as for the 2% ^{57}Fe-doped NiO samples. The spectra appear in figure 11 and the resulting MPs are listed in table 4. The analysis shows the presence of superparamagnetic contributions at the center of the RT spectrum of $NiFe_2O_4$-B together with contributions of broad and

Table 4. Mössbauer parameters as resulting from the best fits of the room-temperature and 77 K spectra of the prepared $NiFe_2O_4$ samples (see the text). (A), (B), (SPM) and (COL) denote A site, B site, superparamagnetic and collapsing, respectively. Typical errors are ± 0.02 mm s^{-1} for $\Gamma/2$, IS, Δ and 2ε, ± 0.5 T for B_{hf} and ΔB_{hf}. The numbers in parentheses for A are standard deviations corresponding to the last digit for each value.

Sample	Temperature	Component	$\Gamma/2$ (mm s^{-1})	IS (mm s^{-1})	2ε or Δ (mm s^{-1})	B_{hf} (T)	ΔB_{hf} (T)	A (%)
$NiFe_2O_4$-A	RT	(A)	0.18	0.26	0.01	49.3	0.4	56.1(3)
		(B)	0.14	0.37	0.00	52.6	0.5	43.9(3)
	77 K	(A)	0.21	0.35	0.01	50.9	0.3	53.2(3)
		(B)	0.18	0.48	0.01	55.4	0.4	46.8(3)
$NiFe_2O_4$-B	RT	(A)	0.27	0.26	0.01	46.6	0.8	19(4)
		(B)	0.15	0.37	−0.01	50.0	1.2	11(3)
		(COL)	0.41	0.31	0.00	41.7	2.1	16(4)
		(COL)	0.31	0.35	0.02	21.0	12.0	32(9)
		(SPM)	0.56	0.32	0.67	—	—	22(5)
	77 K	(A)	0.29	0.38	0.00	50.2	0.3	69.0(6)
		(B)	0.17	0.48	0.01	54.6	0.4	31.0(6)
$NiFe_2O_4$-C	RT	(A)	0.24	0.26	0.01	47.3	0.8	33(2)
		(B)	0.12	0.37	−0.01	50.6	1.2	18(1)
		(COL)	0.23	0.29	−0.08	42.9	3.1	21(2)
		(COL)	0.22	0.35	0.01	23.5	10.8	28(4)
	77 K	(A)	0.25	0.38	0.00	50.5	0.3	63.2(7)
		(B)	0.17	0.48	0.00	54.9	0.4	36.8(7)

collapsing magnetic components, as well as the presence of the characteristic components corresponding to the A and B sites of the 'bulk-$NiFe_2O_4$' phase, with smaller B_{hf} values, relative to the bulk ones [25–27], and broadened resonant lines. In the RT MS of $NiFe_2O_4$-C the superparamagnetic contribution is absent but the broadened, collapsing and 'bulk-$NiFe_2O_4$' magnetic components remain. The RT and 77 K spectra of the $NiFe_2O_4$-A sample show only the characteristic two 'bulk-$NiFe_2O_4$' magnetic components. All superparamagnetic and collapsing magnetic contributions have vanished in the 77 K MS for the $NiFe_2O_4$-B and $NiFe_2O_4$-C samples, where only the high-field A-site and B-site components appear.

The above results indicate that when following the same preparation procedure as for the 2% Fe-doped NiO samples, the $NiFe_2O_4$ phase is definitely formed at 873 K even after 1 h of heat treatment of the corresponding precursor, and includes a range of particle sizes, a part of which are very small in size and behave superparamagnetically at RT. This is in accordance with the corresponding results of the XRD analysis of these $NiFe_2O_4$ samples. Moreover, the formation of crystalline nickel ferrite at the temperature of 873 K is in agreement with the range of crystallization temperatures found for this phase, which has a lower limit of 853 K [46]. However, as the heating time at 873 K increases, the particles grow in size, while if the precursor is heated at elevated temperatures the $NiFe_2O_4$ phase is 'bulk-like' as expected. Thus we can expect to have definite formation of the nickel ferrite phase in our 2% ^{57}Fe-doped NiO samples heated at 873 K in a range of particle sizes, which could include nanoparticles with superparamagnetic behavior at RT, at least for the samples prepared under the shorter heating time conditions, which however grow in size as the heating time increases.

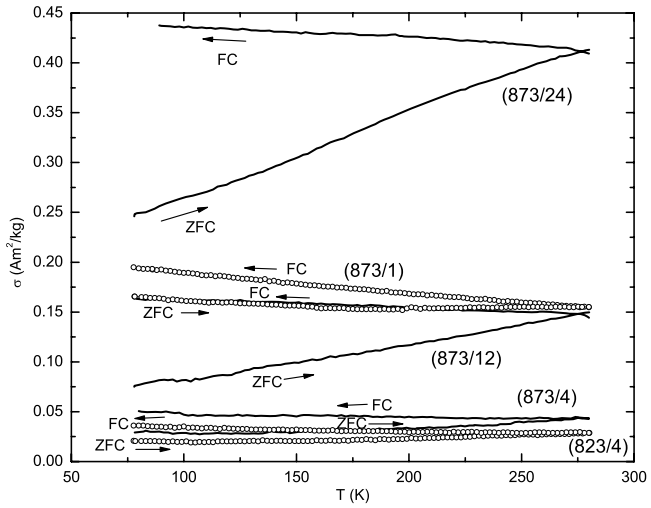

Figure 12. Magnetization versus temperature measurements of the (823/4) and (873/1–24) samples made under an applied magnetic field of 0.1 T. ZFC and FC correspond to zero-field-cooled and field-cooled modes (see the text).

To clarify the presence of superparamagnetic $NiFe_2O_4$ impurities in the (823/4) and (873/1–24) samples we performed magnetization measurements with respect to temperature (σ versus T) under an applied magnetic field of $\mu_0 H = 0.1$ T. The measurements were done in zero-field-cooled (ZFC) and field-cooled (FC) modes from 77 to 280 K, and the results are shown in figure 12. From these measurements it is shown that for samples (873/12) and (873/24) there is no maximum in the ZFC curve, as also no common variation of the magnetization with respect to temperature and a following bifurcation of the ZFC–FC curves at temperatures below 280 K. The two curves just cross for these samples without having a common variation. The maximum in the ZFC curve indicates the average T_B of the system, while the bifurcation temperature points to the maximum T_B corresponding to the largest nanoparticles in the size distribution [33]. The observed behavior means that for these two samples the parameters influencing the dynamic magnetization phenomena of the system (particle volume V and magnetic anisotropy constant K) have such magnitudes as to give a T_B value above 280 K, and probably—according to the shape of the curves—above RT. Although the detection of T_B in a system of nanoparticles depends on the characteristic time of the experimental method used, which is $\sim 10^{-8}$ s for Mössbauer spectroscopy and ~ 1 s for magnetization measurements in the VSM, the two methods agree that T_B is higher than RT for these samples. Thus we expect to see no change in the absorption areas of the $NiFe_2O_4$ phase components at 77 K relative to the RT ones for these samples, because at RT we do not expect to have any superparamagnetic phenomena, and thus no superparamagnetic contribution to the Mössbauer spectra.

For samples (873/1–4) and (823/4) some common variation of the ZFC–FC curves is shown followed by a bifurcation just below 280 K. No maximum magnetization is also observed for the ZFC curves. So in these samples we could expect to have some minor contribution form a superparamagnetic component in the RT MS, which should split magnetically at 77 K. However, as we have already indicated, any contribution of the minor impurity $NiFe_2O_4$ phase components the 77 K spectra is screened out from the major contribution of the dominant ^{57}Fe-doped NiO phase. That is why we have not included any contribution of these components in the analysis of the MS for these samples at this temperature. We could fit the 77 K spectra of

these three samples by including the two high-field components of the $NiFe_2O_4$ phase, but this would impose a very large uncertainty in all their MP values. Thus for the (823/4) and (873/1–4) samples there is an indication of some degree of RT superparamagnetism of the $NiFe_2O_4$ impurity phase, but the amount of this part of the impurity is so small that it cannot be detected by an increase in the absorption area of the $NiFe_2O_4$ Mössbauer components in the 77 K spectra.

4.3. Special features of the $NiFe_2O_4$ impurities

We note that the formation of the $NiFe_2O_4$ impurity in our samples could take place in heating temperatures lower than 873 K, as the presence of this phase is definitely confirmed by the analysis of the RT Mössbauer spectrum and magnetization loop of the (823/4) sample. However, in this case (heating at 823 K) the heating time must be much longer than 1 h in order to achieve the formation of the nickel ferrite impurity, and the amount of this phase formed after heating for 4 h is much lower than the corresponding heating at 873 K (sample (873/4)). Taking this into consideration and combining it with the observation of the gradual increase in the intensity and absorption area of the components corresponding to the $NiFe_2O_4$ phase in the RT MS as the heating time at 873 K increases, we can extract important information on the mechanism of formation of this phase in our 2% ^{57}Fe-doped NiO samples. We suggest that the formation of the impurity $NiFe_2O_4$ phase is related to the diffusion of the $^{57}Fe^{3+}$ ions in stoichiometric $Ni_{0.98}{}^{57}Fe_{0.02}O$, and this process is enhanced with increased heating time and temperature. Furthermore, the nickel ferrite impurity phase produced in the samples must be strongly related to the ^{57}Fe-doped NiO main-phase matrix, and should accordingly interact magnetically with it, as in the case of $NiFe_2O_4$/NiO bilayers [47]. This is an indication which originates from the behavior of the coercivity values with respect to the heating temperature and time in our samples.

In particular, let us assume that there is no magnetic interaction between the impurity $NiFe_2O_4$ phase and the ^{57}Fe-doped NiO main-phase matrix. Then as the particle size of the ^{57}Fe-doped NiO phase increases with increasing heating temperature and time, its magnetization will have a characteristic antiferromagnetic linear dependence with respect to the applied field. So the contribution from this phase combined with a soft-ferromagnetic signal from a $NiFe_2O_4$ impurity phase will give rise to a magnetization loop with very low coercivity, of the order of $\mu_0 H_C \approx 10$ mT, as $NiFe_2O_4$ is a very soft ferrimagnetic phase (see the following). Contrary to that, relatively high $\mu_0 H_C$ values of ≈40–60 mT are found for the 873 K heated samples.

To clarify this issue and in order to have an estimation of the influence of the contribution of the nickel ferrite phase in the magnetization loops of the 2% ^{57}Fe-doped NiO samples, in which this phase has been detected, we made some additional magnetization measurements. We measured the RT magnetization loops of all three prepared $NiFe_2O_4$ samples, as well as of the 0.1 wt% $NiFe_2O_4$-A in NiO mixture sample and of the pure NiO sample. These measurements are shown in figures 13 and 14.

For the nickel ferrite samples, shown in figure 13, the loop of $NiFe_2O_4$-A has a saturation magnetization (σ_S) value of 46 A m^2 kg^{-1}, quite close to the bulk value of 50 A m^2 kg^{-1} [24]. For samples $NiFe_2O_4$-B and $NiFe_2O_4$-C the corresponding values drop to 26 A m^2 kg^{-1}, and 29 A m^2 kg^{-1}, respectively. This decrease is expected due to the reduction of the particle size of these two last samples, which is verified by the XRD and Mössbauer spectroscopy measurements; the decrease also scales with their average particle size. From the inset of figure 13 one can see that the coercivities are around 15 mT and 6 mT for $NiFe_2O_4$-A and $NiFe_2O_4$-B, $NiFe_2O_4$-C samples, respectively. In general the values of σ_S, $\mu_0 H_C$ and the shape of the loop of the $NiFe_2O_4$ phase strongly depend on the preparation procedure followed, and

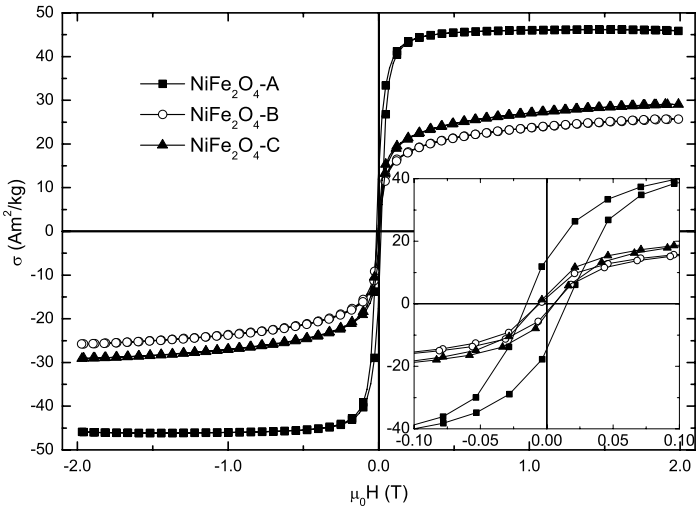

Figure 13. Room-temperature magnetization loops of the prepared $NiFe_2O_4$ samples (see the text). Inset: magnification of the low-applied-field region of the loops.

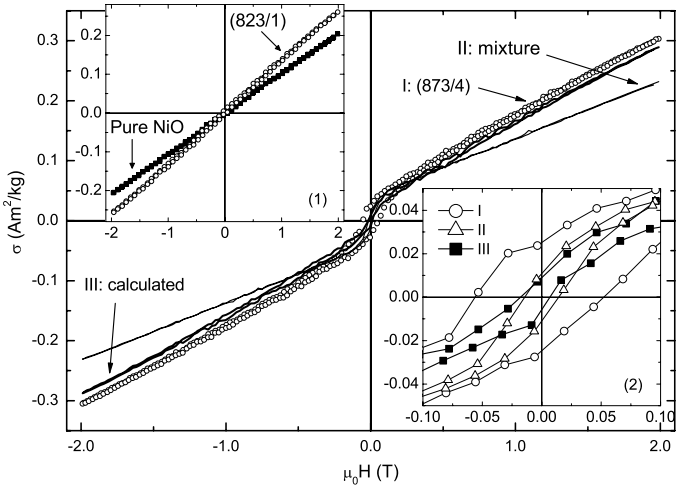

Figure 14. Room-temperature magnetization loops of I: sample (873/4) (open cycles), II: mixture sample of 0.1 wt% $NiFe_2O_4$-A in NiO (thin line), and III: calculated magnetization loop from (823/1) and $NiFe_2O_4$-C samples (thick line)—(see the text). Inset (1): comparison of the room-temperature magnetization loops of pure NiO and (823/1) samples. Inset (2): magnification of the low-applied-field region of the loops I, II and III.

also on the particle size [48–55]. In particular, the features of the magnetization loops of nanostructured $NiFe_2O_4$ relate to finite-size effect phenomena [30–32]. So the σ_S and $\mu_0 H_C$ values found for our $NiFe_2O_4$ prepared samples are in the range of the values expected for particles with sizes 10–50 nm, obtained from a chemical precipitation preparation route. In particular, the range of the detected $\mu_0 H_C$ values of our nickel ferrite samples indicates that they are all magnetically soft materials.

In figure 14 we compare the experimental magnetization loop of the (873/4) sample with that of 0.1 wt% $NiFe_2O_4$-A in NiO mixture sample. We include also in this figure

a calculated magnetization loop resulting from the linear combination of the magnetization loops of the (823/1) and the $NiFe_2O_4$-C samples multiplied by the factors 0.9990 and 0.0010, respectively. We used the (823/1) sample's magnetization loop in this calculation as it is the sample produced with the closest preparation conditions to the (873/4) sample, but is free from any $NiFe_2O_4$ impurity; thus it represents in the best way the pure 'bulk-like' $Ni_{0.98}{}^{57}Fe_{0.02}O$ phase contribution. We also used the magnetization loop of the $NiFe_2O_4$-C sample in this calculation as it is prepared at the same heating conditions as (873/4) and might resemble in the best way the $NiFe_2O_4$ impurity in this sample. We finally used the specific factors because they correspond to the same wt% concentration of the 0.1 wt% $NiFe_2O_4$ in NiO mixture, which is in the range of the concentrations of the $NiFe_2O_4$ impurity in NiO that could not be detected in the XRD patterns. The same fact (undetectable $NiFe_2O_4$ impurities by XRD) stands in the case of the (873/4) sample. Thus we can conclude that we have a $NiFe_2O_4$ impurity concentration in the (873/4) sample which must be at least in the same range of the concentration of $NiFe_2O_4$ in the 0.1 wt% $NiFe_2O_4$/NiO mixture sample.

From the comparison in figure 14 two characteristics are apparent. (i) The high-field magnetization slope of the calculated loop resembles better that of the (873/4) sample, while the corresponding slope of the $NiFe_2O_4$/NiO mixture fails to follow, as it is quite lower. In fact a calculated loop with factors of 0.9985 and 0.0015 for the loops of (823/1) and $NiFe_2O_4$-C samples, respectively, matches exactly the high-field slope of the (873/4) sample loop. This means that the real concentration of $NiFe_2O_4$ phase in the (873/4) sample is indeed in the range of 0.1–0.2 wt%. The failure to reproduce the high-field slope of (873/4) with that of the $NiFe_2O_4$/NiO mixture comes mainly from the difference in the linear antiferromagnetic contribution. As shown in the inset (1) of figure 14, the slope of the linear antiferromagnetic loop of the pure NiO sample is lower than that of sample (823/1), most probably due to the contribution of the participation of Fe ion moments in the latter. (ii) The coercivity of sample (873/4) is higher than those of the calculated and the $NiFe_2O_4$/NiO mixture. This implies that the magnetic anisotropy of the (873/4) sample is higher than the anisotropy of pure $NiFe_2O_4$ produced as a 'stand-alone' phase either at the same preparation conditions or at even higher temperatures.

Thus the observed coercivity values, not only of the (873/4) sample, but for all ^{57}Fe-doped NiO samples prepared at 873 K, are increased compared to those of the pure $NiFe_2O_4$ samples, which are produced following the same preparation route. One could attribute this increase in coercivity to a new source of magnetic anisotropy of the ^{57}Fe-doped NiO system, which originates due to iron doping and does not relate to other known sources like the surface uncompensated spin arrangement, multi-sublattice magnetic structure, or surface broken bond formation described previously. Note here that the latter sources of magnetic anisotropy concern nanoparticles which can be both ^{57}Fe-doped NiO and $NiFe_2O_4$.

To resolve the above argument first, we take into account that the average size of the ^{57}Fe-doped NiO particles, even for the samples heated longer at 873 K, does not cross the 30 nm limit, as indicated by the XRD results. In addition, the suggestion that the $NiFe_2O_4$ impurity phase in our 2% ^{57}Fe-doped samples is formed in sizes that do not cross the range of a few tenths of nanometers, even for the longer-time heated samples at 873 K, is strengthened further by the observed differences in the intensities and absorption areas of the (A) and (B) $NiFe_2O_4$ components of their corresponding RT MS. The intensity and absorption area values of the lower B_{hf} component, which is attributed to the tetrahedral (A-site) Fe ions, are for all samples higher than the corresponding intensity and absorption area of the higher B_{hf} component, which is attributed to the octahedral (B-site) Fe ions (see figure 9 and table 2). Regardless of its origin, which can be attributed to either overpopulation of the tetrahedral A site with Fe^{3+} ions [27], or to a mixed spinel structure due to population of the same site with Ni^{2+} ions [56], this

imbalance is also observed in other $NiFe_2O_4$ nanoparticle systems with sizes down to 8–10 nm, but disappears in particles with sizes around 50–60 nm [27, 56]. So the fact that this imbalance is observed in all MS of our samples in which the ferrite phase is detected, suggests that indeed the average particle size of this impurity phase is in the range of a few tenths of nanometers and in any case does not exceed the ≈50–60 nm limit.

This observation combined with the results of the magnetization measurements of both 2% ^{57}Fe-doped NiO and pure $NiFe_2O_4$ samples implies that the impurity $NiFe_2O_4$ phase produced in our 2% ^{57}Fe-doped NiO samples has special characteristics. These characteristics are not observed for the $NiFe_2O_4$ phase produced following the same route as that for the 2% ^{57}Fe-doped NiO, and appear probably due to the suggested formation of this phase by a diffusion process of the $^{57}Fe^{3+}$ ions from the initial $Ni_{0.98}{}^{57}Fe_{0.02}O$ matrix, or some other similar procedure. Nevertheless, this issue requires further studies focused upon the understanding of the chemical kinetics in this system. In any case $\mu_0 H_C$ values in the range of 30–50 mT at RT have indeed been observed for $NiFe_2O_4$ nanoparticles prepared by the hydrothermal [50] and sol–gel [52] methods.

It follows that the small particle size of the ^{57}Fe-doped NiO phase, and the formation of a 'diffused' ferrimagnetic nanostructured $NiFe_2O_4$ impurity during preparation, favor the establishment of a magnetic coupling between these two phases, on the basis of an exchange bias effect as in the case of $NiFe_2O_4$/NiO bilayers [47]. This coupling gives rise to $\mu_0 H_C$ values for the (823/4) and (873/1–24) samples that are at least in the same range of the ones found for the lower-temperature heated samples (≈ 50 mT), where the $NiFe_2O_4$ phase was not detected at all and the coercivity was of different origin (see section 4.1). Further studies are needed in order to confirm the presence of this coupling, and to investigate any possible exploitations of deliberately produced ferromagnetic impurities in antiferromagnetic materials.

5. Conclusion

Our findings in this work show clearly that even 1 h of heat treatment of the precipitated 2% ^{57}Fe-doped NiO precursor at 873 K would result, beyond any doubt, in the formation of the strong ferrimagnetic $NiFe_2O_4$ impurity phase, although this phase cannot be directly detected by XRD, due to its small particle size and/or high dilution. Thus the ferromagnetism found in our ^{57}Fe-doped NiO samples heated at 873 K cannot be unboundedly attributed to new intrinsic DMS effects, different from the ones found for these kind of particles, which are related either to the appearance of the impurity nickel ferrite phase, or to their reduced particle size (finite-size effects). The increased coercivities found for the 2% ^{57}Fe-doped NiO samples where the impurity $NiFe_2O_4$ phase has been detected is suggested to appear due to an induced anisotropy of this impurity phase related to its magnetic coupling to the antiferromagnetic ^{57}Fe-doped NiO matrix in the frame of an exchange bias mechanism. So as the knowledge of the level and form of impurities in DMS, like the low concentration transition metal-doped binary oxides, play an extremely important role on the justification of their ferromagnetic properties to new intrinsic effects caused by this doping, their full characterization is necessary before further conclusions for the origin of this ferromagnetism can be drawn for these compounds. In particular, the use of the ^{57}Fe Mössbauer spectroscopy technique is essential for the investigation of proposed DMSs containing iron.

Acknowledgments

The use of the XRD, VSM and SEM units of the 'Network of Laboratory Units and Centers' of the University of Ioannina is gratefully acknowledged. This paper is dedicated to our beloved colleague and teacher Professor Vasilis Papaefthymiou.

References

[1] Dietl T, Ohno H and Matsukura F 2001 *Phys. Rev.* B **63** 195205
Fukumura T, Toyosaki H and Yamada Y 2005 *Semicond. Sci. Technol.* **20** S103
Coey J M D and Sanvito S 2004 *J. Phys. D: Appl. Phys.* **37** 988
Katayama-Yoshidaa H and Sato K 2003 *Physica* B **327** 337
Pearton S J, Abernathy C R, Overberg M E, Thaler G T, Norton D P, Theodoropoulou N, Hebard A F, Park Y D, Ren F, Kim J and Boatner L A 2003 *J. Appl. Phys.* **93** 1

[2] Prinz G A 1998 *Science* **282** 1660
Ohno H 1998 *Science* **281** 951
Ohno H 1998 *Science* **291** 840
Wolf S A, Awschalom D D, Buhrman R A, Daughton J M, von Molnár S, Roukes M L, Chtchelkanova A Y and Treger D M 2001 *Science* **294** 1488
Zutic I, Fabian J and Das Sarma S 2004 *Rev. Mod. Phys.* **76** 323
Ohno H, Chiba D, Matsukura F, Omiya T, Abe E, Dietl T, Ohno Y and Ohtani K 2000 *Nature* **408** 944

[3] Matsumoto Y, Murakami M, Shono T, Hasegawa T, Fukumura T, Kawasaki M, Ahmet P, Chikyow T, Koshihara S Y and Koinuma H 2001 *Science* **291** 854
Duhalde S, Vignolo M F, Golmar F, Chiliotte C, Rodríguez Torres C E, Errico L A, Cabrera A F, Rentería M, Sánchez F H and Weissmann M 2005 *Phys. Rev.* B **72** 161313R
Hoa Hong N, Sakai J, Prellier W and Hassini A 2003 *Appl. Phys. Lett.* **83** 3129

[4] Ogale S B, Choudhary R J, Buban J P, Lofland S E, Shinde S R, Kale S N, Kulkarni V N, Higgins J, Lanci C, Simpson J R, Browning N D, Das Sarma S, Drew H D, Greene R L and Venkatesan T 2003 *Phys. Rev. Lett.* **91** 077205
Coey J M D, Douvalis A P, Fitzgerald C B and Venkatesan M 2004 *Appl. Phys. Lett.* **84** 1332

[5] Venkatesan M, Fitzgerald C B, Lunney J G and Coey J M D 2004 *Phys. Rev. Lett.* **93** 177206
Herng T S, Lau S P, Yu S F, Yang H Y, Ji X H, Chen J S, Yasui N and Inaba H 2006 *J. Appl. Phys.* **99** 086101

[6] Yoo Y K, Xue Q, Lee H-C, Cheng S, Xiang X-D, Dionneb G F, Xu S, He J, Chu Y S, Preite S D, Lofland S E and Takeuchi I 2005 *Appl. Phys. Lett.* **86** 042506
Peleckis G, Wang X L and Dou S X 2006 *Appl. Phys. Lett.* **88** 132507

[7] Wei M, Braddon N, Zhi D, Midgley P A, Chen S K, Blamire M G and MacManus-Driscoll J L 2005 *Appl. Phys. Lett.* **86** 072514

[8] Tiwari A, Bhosle V M, Ramachandran S, Sudhakar N, Narayan J, Budak S and Gupta A 2006 *Appl. Phys. Lett.* **88** 142511

[9] Wang J, Cai J, Lin Y-H and Nan C-W 2005 *Appl. Phys. Lett.* **87** 202501

[10] Lin Y-H, Wang J, Cai J, Ying M, Zhao R, Li M and Nan C-W 2006 *Phys. Rev.* B **73** 193308

[11] Sawatzky G A and Allen J W 1984 *Phys. Rev. Lett.* **53** 2339

[12] Cullity B D 1972 *Introduction to Magnetic Materials* (Reading, MA: Addison-Wesley) p 157

[13] Dickson D P E and Berry F J 1986 *Mössbauer Spectroscopy* ed D P E Dickson and F J Berry (Cambridge: Cambridge University Press) pp 1–16

[14] Bahl C R H, Hansen M F, Pedersen T, Saadi S, Nielsen K H, Lebech B and Mørup S 2006 *J. Phys.: Condens. Matter* **18** 4161

[15] Shanker R and Singh R A 1973 *Phys. Rev.* **7** 5000

[16] Rodic D, Spasojevic V, Kusigerski V, Tellgren R and Rundlof H 2000 *Phys. Status Solidi* b **218** 527

[17] Smart J S and Greenwald S 1951 *Phys. Rev.* **82** 113

[18] Bartel L C and Morosin B 1971 *Phys. Rev.* B **3** 1039

[19] Mandal S K, Das A K, Nath T K and Karmakar D 2006 *Appl. Phys. Lett.* **89** 144105

[20] Li L, Chen L, Qihe R and Li G 2006 *Appl. Phys. Lett.* **89** 134102

[21] Cullity B D 1956 *Elements of X-ray Diffraction* (Reading, MA: Addison-Wesley) pp 98–9

[22] Larson A C and Von Dreele R B 2000 *General Structure Analysis System (GSAS) Los Alamos National Laboratory Report LAUR* 86-748

[23] Hill R J 1993 *The Rietveld Method* ed R A Young (Oxford: Oxford University Press) pp 61–101

[24] Cullity B D 1972 *Introduction to Magnetic Materials* (Reading, MA: Addison-Wesley) p 190

[25] Greenwood N N and Gibb T C 1971 *Mössbauer Spectroscopy* (London: Chapman and Hall) pp 266–7

[26] Halasa N A, DePasquali G and Drickamer H G 1974 *Phys. Rev.* B **10** 154

[27] Roy M K and Verma H C 2006 *J. Phys.: Condens. Matter* **18** 7273

[28] Richardson J T and Milligan W O 1956 *Phys. Rev.* **102** 1289

[29] Richardson J T, Yiagas D I, Turk B, Forster K and Twigg M V 1991 *J. Appl. Phys.* **70** 6977

[30] Kodama R H, Makhlouf S A and Berkowitz A E 1997 *Phys. Rev. Lett.* **79** 1393

[31] Kodama R H 1999 *J. Magn. Magn. Mater.* **200** 359
[32] Kodama R H and Berkowitz A E 1999 *Phys. Rev.* B **59** 6321
[33] Makhlouf S A, Parker F T, Spada F E and Berkowitz A E 1997 *J. Appl. Phys.* **81** 5561
[34] Tiwari S D and Rajeev K P 2005 *Phys. Rev.* B **72** 104433
[35] Mørup S 1983 *J. Magn. Magn. Mater.* **37** 39
[36] Dormann J L, Fiorani D and Tronc E 1997 *Adv. Chem. Phys.* **98** 283
[37] Roggwiller P and Kündig W 1973 *Solid State Commun.* **12** 901
[38] Gütlich P, Link R and Trautwein A 1978 *Mössbauer Spectroscopy and Transition Metal Chemistry* (Berlin: Springer) pp 84–7
[39] Mørup S and Hansen B R 2005 *Phys. Rev.* B **72** 024418
[40] Bødker F, Hansen M F, Bender Koch C, Lefmann K and Mørup S 2000 *Phys. Rev.* B **61** 6826
[41] Blume M and Tjon J A 1968 *Phys. Rev.* **165** 446
[42] Afanas'ev A M and Gorobchenko V D 1974 *Sov. Phys.— JETP* **39** 690
[43] Berkowitz A E, Kodama R H, Makhlouf S A, Parker F T, Spada F E, McNiff E J Jr and Foner S 1999 *J. Magn. Magn. Mater.* **196/197** 591
[44] Bødker F, Hansen M F, Bender Koch C and Mørup S 2000 *J. Magn. Magn. Mater.* **221** 32
[45] Mørup S and Topsøe H 1976 *Appl. Phys.* **11** 63
[46] Komatsu T and Soga N 1981 *J. Appl. Phys.* **51** 601
Komatsu T and Soga N 1981 *J. Appl. Phys.* **51** 5926
[47] Negulescu B, Thomas L, Dumont Y, Tessier M, Keller N and Guyot M 2002 *J. Magn. Magn. Mater.* **242–245** 529
[48] Li L-P and Li G-S 2000 *Hyperfine Interact.* **128** 437
[49] Sepelak V, Menzel M, Bergmann I, Wiebcke M, Krumeich F and Becker K D 2004 *J. Magn. Magn. Mater.* **272–276** 1616
[50] Wang J 2006 *Mater. Sci. Eng.* B **127** 81
[51] Chkoundali S, Ammar S, Jouini N, Fievet F, Molinie P, Danot M, Villain F and Greneche J-M 2004 *J. Phys.: Condens. Matter* **16** 4357
[52] Huang X and Chen Z 2005 *Mater. Res. Bull.* **40** 105
[53] George M, John A M, Nair S S, Joy P A and Anantharaman M R 2006 *J. Magn. Magn. Mater.* **302** 190
[54] Kurikka V P, Shafi M, Koltypin Y, Gedanken A, Prozorov R, Balogh J, Lendvai J and Felner I 1997 *J. Phys. Chem.* B **101** 6409
[55] Kodama R H, Berkowitz A E, McNiff E J Jr and Foner S 1997 *J. Appl. Phys.* **81** 5552
[56] Chinnasamy C N, Narayanasamy A, Ponpandian N, Chattopadhyay K, Shinoda K, Jeyadevan B, Tohji K, Nakatsuka K, Furubayashi T and Nakatani I 2001 *Phys. Rev.* B **63** 184108